Micro-structural information of porous materials by optical coherence tomography

ARTICLE *in* MICROPOROUS AND MESOPOROUS MATERIALS · NOVEMBER 2014

Impact Factor: 3.45 · DOI: 10.1016/j.micromeso.2014.07.009

6 AUTHORS, INCLUDING:

Sergio Campello
Federal University of Pernambuco
10 PUBLICATIONS **49** CITATIONS
SEE PROFILE

Wellington Pinheiro Dos Santos
Federal University of Pernambuco
42 PUBLICATIONS **72** CITATIONS
SEE PROFILE

Cláudia Cristina Brainer de Oliveira Mota
19 PUBLICATIONS **54** CITATIONS
SEE PROFILE

Anderson S L Gomes
Federal University of Pernambuco
328 PUBLICATIONS **3,697** CITATIONS
SEE PROFILE

Microporous and Mesoporous Materials 198 (2014) 50–54

Contents lists available at ScienceDirect

Microporous and Mesoporous Materials

journal homepage: www.elsevier.com/locate/micromeso

Micro-structural information of porous materials by optical coherence tomography

S.L. Campello [a,*], W.P. dos Santos [b], V.F. Machado [c], C.C.B.O. Mota [d], A.S.L. Gomes [e], R.E. de Souza [e,*]

[a] Núcleo de Formação Docente, Universidade Federal de Pernambuco, 55014-900 Recife, PE, Brazil
[b] Departamento de Engenharia Biomédica, Universidade Federal de Pernambuco, 50670-901 Recife, PE, Brazil
[c] Cenpes, Cidade Universitária, 21941-915 Rio de Janeiro, RJ, Brazil
[d] Graduate Program in Dentistry, Universidade Federal de Pernambuco, 50670-901 Recife, PE, Brazil
[e] Departamento de Física, Universidade Federal de Pernambuco, 50670-901 Recife, PE, Brazil

ARTICLE INFO

Article history:
Received 23 April 2014
Received in revised form 27 June 2014
Accepted 9 July 2014
Available online 17 July 2014

Keywords:
Optical coherence tomography
Porous media
Image processing
Pore size distribution

ABSTRACT

In this study we describe the use of optical coherence tomography (OCT) to reveal microstructures and damages in porous media. An approach for establishing pore size and pore size distribution based upon OCT was developed. This approach was tested with oil source rock samples. Several sedimentary rock samples from Brazilian oil fields with porosity values ranging between 15% and 28% were evaluated, and the results agreed quite well with the traditional pycnometry method. In addition, pore size distribution for the samples in three dimensional planes were obtained. Finally, the experimental results proved that the OCT images with a suited digital post-processing can be used to measure pore size distribution in natural and artificial materials, with the advantage of being non-invasive, faster and much less expensive than other presently available methods.

1. Introduction

Optical coherence tomography (OCT), introduced by Huang et al [1], is a technique based on interference phenomena using broadband light sources or frequency swept optical sources. A back-reflected reference light beam and a backscattered light beam from the sample are combined to produce a low coherence interferometric pattern data, which are mathematically processed to generate the OCT image. This technique enables the generation of in situ 2D and 3D images of transparent and nontransparent samples [2] with micro-scale resolution. The main characteristics of this technique that have made OCT images successful are: low cost, contact-free, and non-invasive character.

Due to these characteristics, OCT technique has been mainly used in biomedicine. First applications of OCT were in Ophthalmology, focused on retinal disease [3]. In order to get OCT images from nontransparent tissues, the optical window was moved from 800 nm to 1300 nm, allowing *in vivo* diagnostics of other part of human body [4–6]. For a recent review on OCT and its multidisciplinary applications, see Ref [7].

Since the technique allows the visualization of microstructure within highly scattering media, several applications outside biomedical field have started to come out. First applications of OCT were in ceramic materials research, such as void structures detection as a function of depth in silicon nitride ceramics [8]. Polymer sheets and polymer based coatings were already studied using OCT techniques [9]. OCT experiments were also performed on paper, which is a highly heterogeneous system that contains fibers, fiber fragments and additives. This structure imposes depth limits that depend on paper composition. Several works presented characterization of paper surface and bulk structure [10,11].

The results from the works mentioned above suggest a new non-biomedical application of OCT for characterization of porous media. Among the most important technological porous materials are rocks from oil fields. The modern oil industry needs increasingly accurate information about the collected oil source rock samples. In order to assess the cost/benefit ratio of a given oil field before beginning the exploration, an important parameter to be considered is the available oil volume that can be extracted. An important part of information needed to estimate this volume is the pore size distribution. However, most of the techniques for pore size distribution measurements are invasive – and therefore destructive, expensive, relatively time-consuming, and/or do not have enough resolution.

In this work, it is presented the application of OCT to microstructure study in porous media. As reported in applications for paper studies [9,10], a judicious digital image processing including filtering methods is quite important to get quantitative results. The images were obtained using a commercial OCT system and 13

* Corresponding authors.
E-mail address: slcampello@df.ufpe.br (S.L. Campello).

http://dx.doi.org/10.1016/j.micromeso.2014.07.009
1387-1811/

samples of rock from Brazilian oil fields were analyzed. The obtained results indicate that application of OCT images to obtain pore structure and pore size distribution in samples is feasible, opening up possibilities as an affordable and fast evaluation method.

2. Materials and methods

2.1. Samples

The porous media used in this investigation are rock specimens and were furnished by PETROBRAS (Petroleum Brazilian State Company), which were sampled from several different field locations. A group of 13 cylindrical samples were approximately 50 mm long and 40 mm in diameter. They were classified into 4 subgroups according to geographic location. The samples were washed several times to ensure that there was no oil or salt content. Fig. 1 shows some samples and Table 1 presents sample distribution in subgroups and their respective porosity (Φ_{pyc}) obtained by helium gas expansion (pycnometry) in a CoreLab UltraPore Porosimeter. The last column shows the $\Phi_{pyc} \pm \Delta\Phi_{pyc}$ values.

2.2. OCT instrumentation

An OCT system OCP930SR model from THORLABS was used. The system is multipurpose, although mainly designed for biological applications like *in vivo* human skin images. It operates at 930 nm and with a spectral width of 30 nm, an output power of 2 mW and axial resolution of 6 μm. This system combines a broadband light source with a high-speed spectrometer to perform a Fourier domain detection of the OCT interference fringe signals. The base unit includes the broad super luminescent diode (SLD) light source, the spectrometer, analog and digital timing circuitry, and drive electronics for the galvanometer scanner within the probe. A PC controls data measurement, collection, processing, displaying and managing OCT image files. The images were saved as numeric array matrix and composed by 2000 columns and 512 lines, providing a pixel resolution of 3 μm × 3.1 μm. Each cross-sectional image is a "B-scan" composed of several "A-scans" (columns).

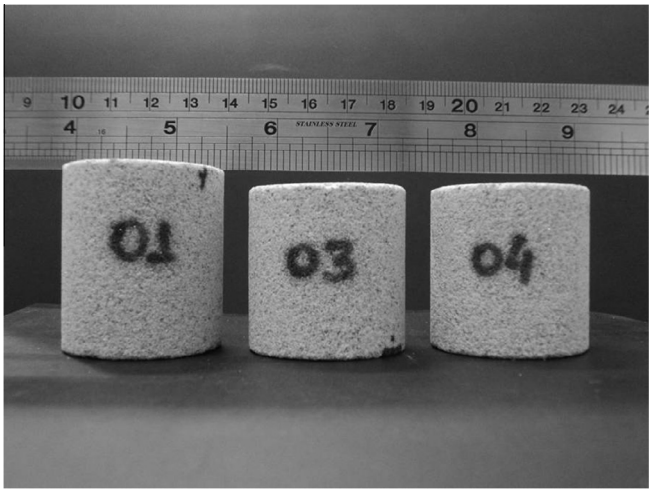

Fig. 1. Samples of the subgroup 1.

2.3. OCT method description

For each sample at least 100 B-scans were obtained from the circular base of all samples separated by 50 μm. Since samples are strongly scattering porous media, two complementary algorithms of image processing were developed in order to obtain quantitative information from OCT images. The aim of the image processing is to obtain a binary image, which contains structural information about porosity and pore size distribution. Porosity is defined as the ratio $\Phi = V_P/V$, where V_P and V are the porous volume and total volume of the sample, respectively. Void areas in OCT images of our samples are considered porous space. For a two dimensional version one can write porosity as:

$$\Phi = A_v/A \quad (1)$$

where A_V and A are the void and total area of the image, respectively. In this case, area is measured in number of pixels of the OCT image.

The image processing is divided in two parts. Initially, the first algorithm determines the optimized threshold value for a given porosity. Then, all images are binarized with the optimal threshold value and the pore size distribution is obtained in the second algorithm.

Fig. 2 shows an OCT image without any image processing. One can easily see the speckle noise effects and the signal decay through depth (lines). In general, OCT images of rocks present speckle noise. The first algorithm is started with the original image and step A is to filter out as good as possible the noise. Due to light absorption and scattering, light intensity decreases as the light penetrates into the rock sample. In order to clarify this statement, Fig. 3 shows the averaged OCT signal intensity decay for image as

Table 1
Subgroups of samples, individual porosity values Φ_{pyc} obtained by helium gas porosimeter, values with uncertainty $\Delta\Phi_{pyc}$. After image processing, sample average threshold values ($\bar{t}$) and respective standard deviation (σ_t), porosity ($\bar{\Phi}_{OCT}$) and standard deviation values ($\Delta\Phi_{OCT}$) were obtained.

Subgroup number (dominant rock color)/ Sample code		Φ_{pyc} (%)	$\Phi_{pyc} \pm \Delta\Phi_{pyc}$ (%)	$\bar{t}$	σ_t	$\bar{\Phi}_{OCT}$	σ_Φ	$\bar{\Phi}_{OCT} \pm \Delta\Phi_{OCT}$ (%)
1 (gray)	01	22.15	22 ± 1	0.3594	0.02	0.2219	0.04	22 ± 4
	03	21.08	21 ± 2	0.3556	0.03	0.2097	0.04	21 ± 4
	04	22.11	22 ± 2	0.3592	0.03	0.2242	0.05	22 ± 4
2 (gray)	4-5B	23.48	23 ± 2	0.3356	0.02	0.2380	0.04	24 ± 4
	6-2B	22.11	22 ± 2	0.3493	0.02	0.2235	0.03	22 ± 3
	10-2B	21.61	22 ± 2	0.3703	0.03	0.2189	0.05	22 ± 5
3 (red)	R266	17.46	17 ± 2	0.3994	0.02	0.1745	0.03	17 ± 3
	R267	19.21	19 ± 1	0.4209	0.03	0.1949	0.04	19 ± 4
	R268	17.64	18 ± 2	0.4120	0.02	0.1768	0.03	18 ± 3
4 (red)	L2	17.13	17 ± 1	0.3896	0.03	0.1727	0.03	17 ± 3
	L3	17.01	17 ± 1	0.4137	0.03	0.1707	0.03	17 ± 3
	L4	16.90	17 ± 1	0.4238	0.02	0.1701	0.03	17 ± 3
	L5	16.49	16 ± 1	0.3940	0.03	0.1685	0.05	17 ± 5

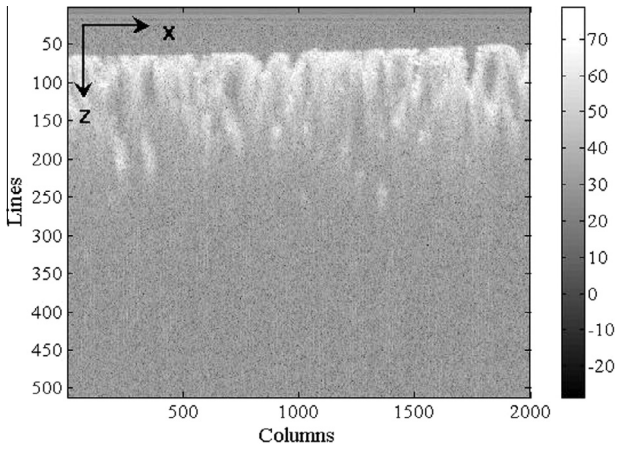

Fig. 2. Image obtained from OCT system without processing. The x and z axis scanning correspond respectively to 6.0 mm and 1.5 mm.

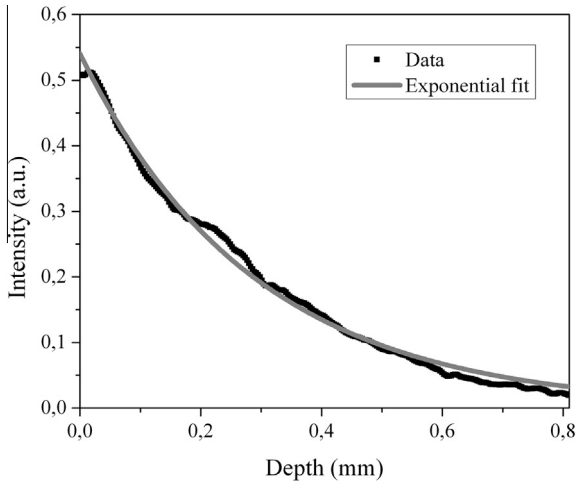

Fig. 3. Average signal decay (■) obtained after image filtering and the fitting using Beer function (—).

function of depth, after step A. Steps B, C, and D perform a signal compensation assuming a Beer–Lambert–Bouguer law decay of the averaged of A-scans. The fitting result is the gray line in Fig. 3. The signal recovery is executed by multiplying each column by an exponential growth function similar to Eq. (2):

$$I'(z) = I_0 \exp(+2\alpha z) \tag{2}$$

where $I'(z)$ is the intensity as a function of depth z and α is the optical attenuation coefficient obtained by fitting the light intensity decay. The image obtained in D step has an approximately homogeneous signal as a function of depth.

Step E executes an image binarization using an initial threshold value (t_0) that will be optimized. Hereafter step F leads to the porosity calculation applying Eq. (1). At this stage it is obtained slice porosity values. Next steps G, H, and I, are a loop that optimizes threshold value comparison with porosity values obtained by pycnometry measurements. This calibration will always be required for at least one sample in the group to be measured. For the particular case of rock oil samples, different rocks will require different calibration. For the execution of the algorithm, it ends when an OCT porosity value close to Φ_{pyc} within predefined error $\varepsilon \leqslant 0.05$ is obtained. After all OCT image processing each image has an associate optimized threshold value and all values are stored in a vector (vector T).

The purpose of the second part is to obtain the porosity and the pore size distribution from all binary images. In step J, it is calculated the average value $\bar{t}$ of thresholds stored in the vector T. The $\bar{t}$ is then used to binarize all images, step K, followed by step L that calculates the porosity values of all images individually. Step M makes an image reconstruction in order to correct possible artifacts produced in steps B, C and D because it is made a boundary linearization on the steps previously related to measure the decay signal of light. Finally, step N performs the count of pores and the pore size of each one.

3. Results and discussion

Fig. 4 presents porosity values obtained from sample 01 for each slice. Variations of the porosity among slices are observed. This result seems to indicate the sensibility of the method to detect structural differences between small translations in a sample. This sensibility is also characterized by the difference among the porosity values of the samples from groups 1 and 2 and the groups 3 and 4. The porosity values as function of slice position has a curious behavior that deserves further investigation. Porosity is almost constant for several slices and suddenly varies within few slices, and then resumes to the original values. This behavior is repeated, however, not periodically. It can suggest different periods of sedimentation under different conditions.

In Table 1 all significant values used for image processing and calculated quantities are presented. It also shows the average threshold $\bar{t}$ of each subgroup used to binarize all images as explained in Section 2.3 and its standard deviation. Results in Table 1 compared with the porosity values by pycnometry show that the threshold values, found with the presented algorithm, provide porosity values which are very close to pycnometry values.

In order to visualize the performance of the OCT method, OCT porosity values were plotted against pycnometric porosity values together with the $y = x$ curve, shown in Fig. 5. The error bars of Φ_{OCT} and Φ_{pyc} axis are respectively the standard deviation and the experimental uncertainty (see Table 1). It can be observed that OCT porosity is systematically slightly greater than porosity by pycnometry. However, this trend apparently does not depend on a specific subgroup.

In the last part of the image processing it is performed the counting of pores and the measurement of pore sizes on binary images. A pore size distribution is obtained and results for subgroup 4 are presented in Fig. 6. All samples present distributions with similar behavior. Fig. 6 reveals two quite distincts distributions of pores. The first one with a huge number of smaller pores

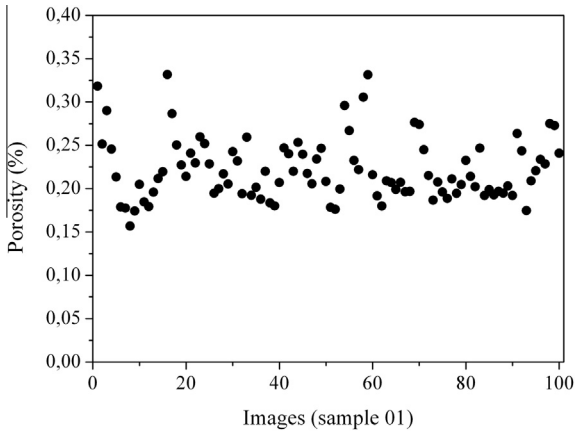

Fig. 4. Local porosity for each image in sample 01. The images are separated by 50 μm, which means that a region of 30 mm^2 is scanned.

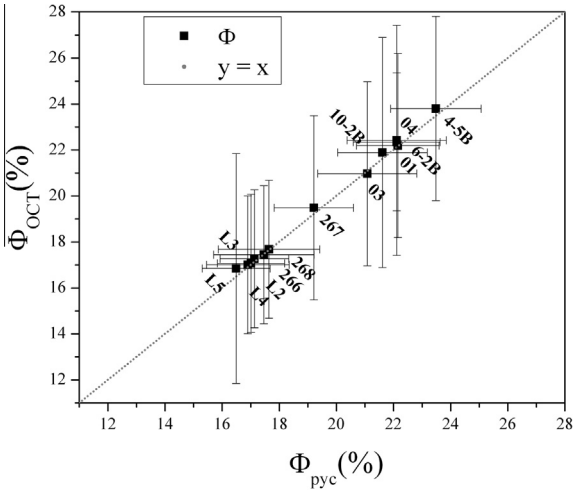

Fig. 5. Comparison between porosities Φ_{OCT} and Φ_{pyc}.

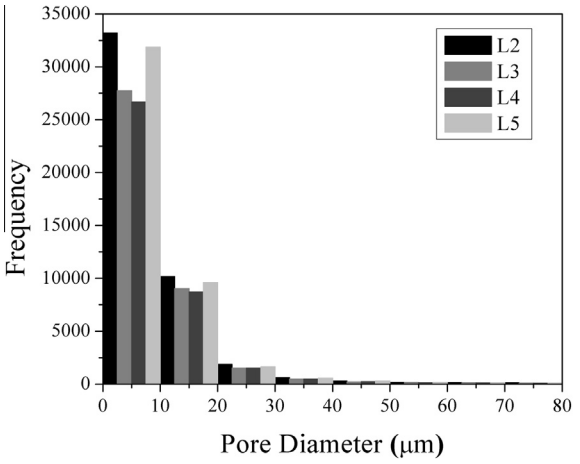

Fig. 6. Pore size distribution of subgroup 4.

is broad in size distribution. Another distribution with a small number of bigger pores is narrow in pore size distribution. The two distribution occupy two quite separated regions in size range. The second one is not present at the beginning of the sedimentation process. At the initial stages of sedimentation process, although liquid in the pores tend to balance pressures between differents regions, this balance depends on the connectivity between pores. Therefore, in regions with low connectivity, huge non uniforme pressure gradients can occur, which can conduct to the local structural collapses. These collapses give rise to huge pores forming the second distribution mentioned, which has some characteristics which are totally different from the first one.

In Fig. 6, it is shown only the first pore size distribution mentioned above. The second one appears in a much higher pore diameter range. Fig. 6 shows approximately the same pattern of frequencies within each bin. Besides, that average frequency within each bin, approximately decreases linearly as a function of pore diameter. It is not found in the literature similar measurements to compare to these results. It is found pore size distribution in oil source rocks obtained by low field NMR relaxation measurements [11]. However, this kind of measurements is an indirect method, which does not access this range of size, and strongly depends on the rock type.

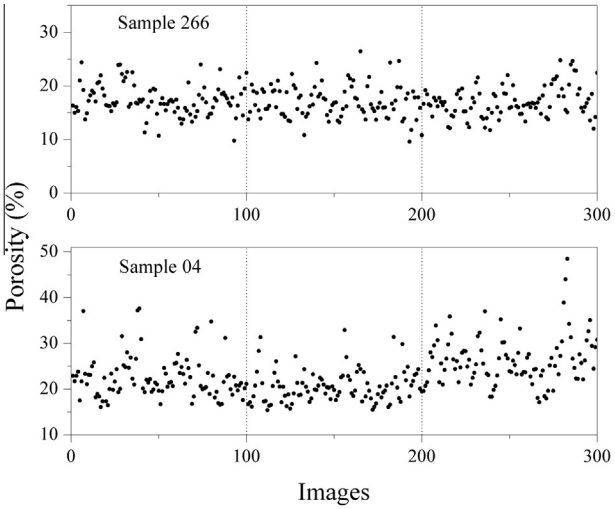

Fig. 7. Porosity obtained in planes *xz* (1–100), *yz* (101–200) and *xy* (201–300) to verify isotropy.

The calculation of porosity and pore diameter were based on two-dimensional images extracted from a plane of samples. However, porosity is a quantity that involves a volume ratio and it contains information about the three-dimensional distribution of the sample material. Thus, it is necessary to verify if the measurements with image processing obtained by OCT produce similar results on other planes of the samples, i.e., if the results do not depend on the direction of the measurement plane.

In order to verify the 3D information, 100 images from each plane of the rock: *xz*, *yz* and *xy* were obtained. Then, all images underwent the same process previously described in Section 2.3, which lead to the optimal threshold for each plane. Then, the optimal threshold of 100 images from the *xz* plane is used to binarize all 300 images of the three planes. The results obtained for samples 266 and 04 are presented in Fig. 7.

Results from sample 04 shows that porosity values in *xy* plane slightly differ from the other planes. This result can be explained by the cutting processes being different on sample surface and lateral. The cutting process did not affect the sample 266 because of its higher hardness and also because this sample can be considered as isotropic.

Presented in Table 2 are the porosity results of subgroups 1 (samples 01, 03 and 04) and 3 (samples 266, 267 and 268) for 300 images. In comparison with values in Table 1, we could consider the samples as isotropic because of its low absolute error values.

The technique used as reference provides a single value of the porosity, i.e., a macroscopic information of pore volume. The method developed here is capable of obtaining a distribution of the porosity values, indicating the sensitivity of the method to detect local changes in sample. For example, Fig. 8 presents the porosity distribution values in sample 03.

Table 2
Average porosity values after image processing with 100 images acquired in each of 3 planes of samples to verify isotropy in samples.

Sample	$\bar{\Phi}_{total} \pm \sigma_{\Phi total}$ (%)
01	24 ± 5
03	23 ± 5
04	23 ± 5
266	17 ± 3
267	18 ± 4
268	17 ± 3

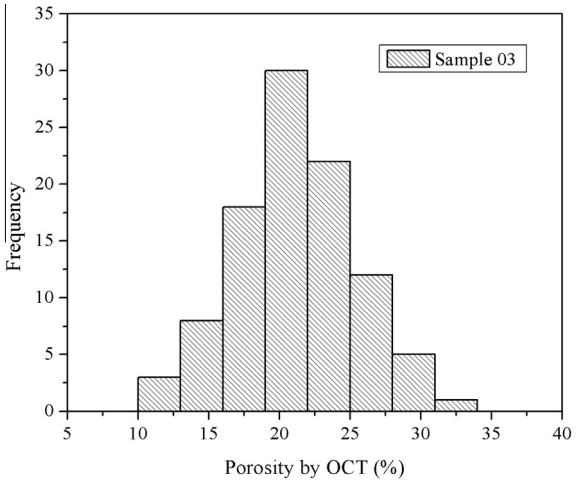

Fig. 8. Porosity distribution obtained by OCT measurements for sample 03.

4. Conclusion

The results obtained by the image processing indicate that the OCT technique can be used to obtain the pore size distribution in porous materials, as demonstrated for petroleum source rocks, which was the original aim of this work. Besides being non-invasive, non-destructive, cheaper, and faster than most of techniques, the advantage of the proposed and demonstrated method is its sensitivity to local microstructural information. Although at the current stage the method requires an input related to the porosity of the material, this input is a volumetric feature of the sample. Starting from this input, however, the method can produce results that reveal microstructural details, opening up avenues for several applications in porous media.

Acknowledgments

The authors would like to thank Dr. B. Kyotoku for several enlightening discussions and Mrs A. Linda for the grammar review. Financial support from CAPES, CNPq and FACEPE, Brazilian Agencies, are gratefully acknowledged. This work was also supported by the INCT Photonics and PRONEX Program, FACEPE/CNPq.

References

[1] D. Huang et al., Science 254 (5035) (1991) 1178–1181.
[2] M.E. Brezinski et al., Circulation 93 (6) (1996) 1206–1213.
[3] E.A. Swanson et al., Opt. Lett. 18 (21) (1993) 1864–1866.
[4] M.E. Brezinski et al., Am. J. Cardiol. 77 (1) (1996) 92–93.
[5] J.M. Schmitt, M.J. Yadlowsky, R.F. Bonner, Dermatology 191 (2) (1995) 93–98.
[6] G.J. Tearney et al., Science 276 (5321) (1997) 2037–2039.
[7] B. Bouma, Handbook of Optical Coherence Tomography, Taylor & Francis, 2001.
[8] M. Bashkansky et al., J. Am. Ceram. Soc. 79 (5) (1996) 1397–1400.
[9] M. Duncan, M. Bashkansky, J. Reintjes, Opt. Express 2 (13) (1998) 540–545.
[10] E. Alarousu et al., Meas. Sci. Technol. 16 (5) (2005) 1131–1137.
[11] T. Fabritius et al., Quantum Electron. 36 (2) (2006) 181–187.